

Influence of Al-doped SrTiO₃ cores on hydrogen evolution from SrTiO₃/TiO₂ core-shell catalysts

Wenjia Song, Paul A. Salvador, and Gregory S. Rohrer*

Department of Materials Science and Engineering, Carnegie Mellon University, Pittsburgh, Pennsylvania 15213, United States.

*Corresponding author: E-mail: gr20@andrew.cmu.edu

[Accepted for publication, Journal of the American Ceramic Society, 2025](#)

Abstract

The hydrogen produced by Al-doped SrTiO₃/TiO₂ core-shell catalysts with a range of Al-doped SrTiO₃ cores and the same TiO₂ shell are compared. The study included SrTiO₃ cores doped with different amounts of Al (0, 1, 2, or 3 mole percent) added at different points in the synthesis (prior to or during the molten salt treatment) and at different temperatures (900, 1000, and 1100 °C). It was found that core-shell catalysts with different cores had hydrogen generation rates that varied by a factor of more than 40 and varied with the processing parameters in the same way as the hydrogen generation rates of the cores alone. The best catalysts had 2 or 3 mole percent added Al, added during treatment in a SrCl₂ molten salt at 1000 °C or 1100 °C. Because the core absorbs most of the light, its ability to separate and transport photogenerated charge carriers dominates the properties of the core-shell catalyst. This indicates that, to optimize the properties of core-shell catalysts, it is essential to optimize the properties of the core. While the shell can be important to protect the core from degradation, it is not as important to the overall reactivity as the core.

Keywords: photocatalyst, water splitting, SrTiO₃, core-shell structure

1. Introduction

Certain metal oxides can be used as photocatalysts to split water to yield hydrogen, a fuel that could potentially be used to decarbonize energy production.^{1,2} Heterostructured core-shell photocatalysts, consisting of a light absorbing core coated with a catalytically active shell, have been used to independently adjust the properties of the bulk and surface-active phases.^{3,4} This makes it possible to separately optimize the core for light absorption and the transport of photogenerated charge carriers, and the shell for surface area, stability against corrosion,⁵ and band bending. A typical structure includes a bulk core material in the 0.1 to 2 μm size range and a thin supported shell layer with a thickness of 10 to 100 nm.⁶⁻⁹ One interesting class of such heterostructured composites includes oxide cores and shells of titania.^{3,4,10} Titania is stable with respect to photocorrosion and can protect cores that would otherwise degrade.⁵ These materials can be produced using a sol-gel synthesis of titania in the presence of the already crystalline core particles.^{11,12} The composite structure must then be annealed to crystallize the titania. A study of $\text{SrTiO}_3/\text{TiO}_2$ core-shell particles illustrated that there is an ideal annealing temperature that is large enough to form a crystalline interface between the core and the shell, but not so large that the shell coarsens and loses significant surface area or dewets.¹³ Past work has focused on the processing of the shell, exploring parameters such as thickness, annealing temperature, titania phase, and surface activation.³ Many oxide phases have been explored for the cores, including, but not limited to: tourmaline,¹⁴ FeTiO_3 ,¹⁵ BaTiO_3 ,¹¹ PbTiO_3 ,¹² SrTiO_3 ,¹¹ and BiFeO_3 .¹⁶ While the phase of the core, because of its bandgap, clearly impacts photocatalytic properties, much less is known about how variations of the core preparation and doping concentration impact the properties of the composite catalyst when the shell characteristics are fixed.

One of the early core-shell catalysts that was studied was SrTiO₃/TiO₂, which showed interesting properties under UV illumination.¹¹ However, no efforts were made to optimize the SrTiO₃ core. More recently, it has been discovered that Al-doped SrTiO₃, treated in molten SrCl₂, is a remarkable photocatalyst for water splitting.¹⁷⁻²⁰ In fact, with appropriate co-catalysts applied selectively to different faces of polygonal particles, Al-doped SrTiO₃ can split water with near unit efficiency in 365 nm light.²¹ The photocatalytic properties of Al-doped SrTiO₃ have been shown to vary with the amount of Al-doping,¹⁸ particle size and shape,²² and the details of the SrCl₂ treatment.²³ Because of this, it is an excellent material to test the effect of the core properties on the properties of the composite catalyst.

The purpose of this work was to determine how the characteristics of a variety of Al-doped SrTiO₃ cores influence the properties of SrTiO₃/TiO₂ core-shell composites. While water splitting by SrTiO₃/TiO₂ composites was reported earlier,^{11,13} these studies were carried out before the beneficial effects of Al-doping and the SrCl₂ molten salt treatment were recognized. Relying on the previous work,¹³ we fix the processing conditions of the shell material, using parameters that led optimized reactivity. We vary the cores by adding different amounts of Al (0, 1, 2, or 3 mole percent) and at different points in the synthesis (prior to or during the molten salt treatment) and at different temperatures (900, 1000, and 1100 °C). A comparison of the trends in the hydrogen yield from the cores alone and from the core-shell catalyst shows that the two are closely related and that more reactive cores yield more reactive core-shell catalysts. Depending on the characteristics of the SrTiO₃ core, the hydrogen production rates can vary by a factor of more than 40, highlighting the importance of the core material. In fact, for the most reactive cores, the shell does not significantly increase the reactivity and serves only as a protective layer.

2. Experimental Methods

2.1 Preparation of Al-doped SrTiO₃ in molten salts

SrTiO₃ (Aldrich), Al₂O₃ nanopowder (Sigma-Aldrich, <50 nm particle size), and KCl (Alfa Aesar, or SrCl₂ (CERAC, inc.)) with molar ratios of 1:0:10, 1:1:10, 1:2:10, or 1:3:10 were ball milled for 3 h using YSZ balls as grinding media and ethanol as lubricant. The mixtures were then magnetically stirred for 2 h and dried overnight. Each of the four mixtures was then split evenly into three parts and annealed at 900 °C, 1000 °C, and 1100 °C for 10 h in aluminum oxide crucibles with an excess of SrCl₂. Afterwards, the mixtures were washed in boiling DI water to remove the SrCl₂. A few drops of 0.1 M AgNO₃ (Acros) solution were added into the wastewater and there was no observable precipitation. After washing, the powders were dried overnight. The 24 powders are labeled in the following way: the first letter, S (K), specifies the molten SrCl₂ (KCl) salt treatment. The second digit, 0, 1, 2, or 3, represents the molar ratio of Al₂O₃ to SrTiO₃ being 0 %, 1 %, 2 %, or 3 %. The last numbers, 9, 10, or 11, represent the annealing temperatures, 900 °C, 1000 °C, or 1100 °C, respectively.

2.2 Solid state preparation of Al-doped SrTiO₃

A parallel set of samples was synthesized with the aim of dissolving the Al into SrTiO₃ prior to the SrCl₂ treatment. For this synthesis, an aluminum containing precursor was precipitated onto the SrTiO₃ powder, and the mixture was then annealed in the solid state. Specifically, SrTiO₃ powders were suspended in aqueous Al(NO₃)₃ (Sigma-Aldrich) solutions with concentrations to yield 0, 1, 2, and 3 mole percent Al and then stirred for 0.5 h before drying. The dried powders were then compressed to form 1-cm-diameter pellets using a force of 10,000 lbs and a few drops of PVA as a binder. The pellets were annealed at 1000 °C for 10 h to homogenize the Al

distribution. After cooling, the pellets were ground and the powders were placed in an aluminum oxide crucible with an excess of SrCl_2 and heated at $1000\text{ }^\circ\text{C}$ for 10 h. The powders were then washed to remove the SrCl_2 and dried. These powders were named in the same way as the previous ones, except that they are prefixed with “ss-” to indicate that Al was added in the solid state. Therefore, the four samples are labeled ss-S010, ss-S110, ss-S210, and ss-S310.

2.3. Preparation of core shell particles

Selected SrTiO_3 powders were coated with TiO_2 using a previously described sol-gel method.^{11,13} Simply described, a sol-gel synthesis of TiO_2 is carried out in the presence of SrTiO_3 powder. Briefly, 0.5 g SrTiO_3 powder was added to a mixture containing 10 ml ethanol and 4.5 ml DI water and stirred for 0.5 h. A few drops of HCl (Fisher Scientific) was then added to the suspension to adjust the pH to ~ 3 . Another solution was prepared by mixing 7.5 ml ethanol, 4.3 ml titanium(IV) n-butoxide (Fisher Scientific), and 0.5 ml 2,4 pentanedione (Sigma-Aldrich); this solution was then added drop wise to the stirred suspension. Next, the mixture was stirred for 2 h before being heated under reflux at $\sim 90\text{ }^\circ\text{C}$ for 3 h. The product was collected by centrifugation and washed three times with ethanol. A diffraction pattern of this material is included in Fig. S1. The gel coated SrTiO_3 was dried and annealed at $600\text{ }^\circ\text{C}$ for 2 h for the crystallization of the TiO_2 coating. The letter “T” is added to the end of the label of all the particles coated with TiO_2 . A free-standing TiO_2 shell was synthesized using the same method, but without any added SrTiO_3 ; this material is labeled with the suffix “s”. The conditions were selected based on the results of earlier optimization studies.¹³ It was found that this yields a shell that is about 100 nm thick, is comprised of 92 % anatase with the balance rutile, and a specific surface area of $44\text{ m}^2/\text{g}$. Higher annealing temperatures lead to conversion to rutile and a loss of

surface areas, while lower temperature annealing is thought to produce a SrTiO₃/TiO₂ interface of insufficient quality for charge transfer from the core to the shell.¹³

2.4. Addition of co-catalysts

Depending on the type of catalyst, two different co-catalysts were used. If the outer surface of the material was SrTiO₃, RhCrO_x was used as a co-catalyst.²⁴ If the outer surface was TiO₂, then Pt was used. RhCrO_x (1 wt% Rh and 1 wt% Cr) was added to the SrTiO₃ surface by the hydrolysis of the corresponding salts. For this process, appropriate amounts of Na₃RhCl₆ (Sigma-Aldrich) and Cr(NO₃)₃ (Sigma-Aldrich) were dissolved in DI water; 1 ml of this solution was then added to 0.1 g of prepared SrTiO₃ in an evaporation dish. The suspension was then heated in a hot water bath while being stirred with a glass rod until it dried. Next, the powder was transferred into an alumina crucible and annealed at 350 °C for 1 h to allow crystallization of the oxide co-catalyst. The catalysts with outer surfaces of TiO₂ were impregnated with 1 wt.% Pt by the chemical reduction of H₂PtCl₆.²⁵ First the catalyst was added to a H₂PtCl₆ (Sigma-Aldrich) solution and stirred for 2 h for impregnation, and then the Pt⁴⁺ was reduced by adding five-fold excess of NaBH₄ (Acros) and NaOH (Acros Organics) solution and stirring for 2 h. The products were collected by centrifugation, washed with DI water, and dried overnight.

2.5. Measurements of hydrogen evolution

The rate of hydrogen evolution from each catalyst was measured using a parallelized and automated photochemical reactor (PAPCR).²⁶ In this experiment, up to 100 catalysts can be tested simultaneously by illuminating an array of 1.1 ml glass shell vials containing catalysts and water and monitoring the concentration of hydrogen in each vial colorimetrically. Because each reactor is covered by a hydrogen sensitive material (DetecTape, Midsun Specialty Products) that darkens in proportion to the hydrogen concentration, periodically acquired digital images can be

analyzed to determine the hydrogen concentration with time. To quantify the measurements, the color response of the hydrogen sensitive material is calibrated by adding different, but known amounts of hydrogen to a set of reactors and measuring the color change. This calibration curve is then used in the experiment to translate the observed color to an amount of hydrogen in the reactor. The darkening of the hydrogen sensitive material is approximately linear with the hydrogen concentration in the range of 5 % to 40 % H₂ in the headspace of each glass vial. In this work, two different reactors with different calibration curves were used, but both yielded the same hydrogen production rates for the same catalysts, within the uncertainty of the measurement. More detailed descriptions of this reactor and the data processing method have been provided in previous studies.^{22,27}

For the current measurements, the catalyst and water whose pH was adjusted by NaOH or HNO₃ solutions (Fisher Chemical) was added to the 1.1 ml glass shell vials. In nearly every case, each vial had 6.4 mg of catalyst and 0.4 ml of water; instances with different amounts are noted when relevant. In some cases, an aqueous solution with 8 vol.% methanol was used and these cases are labeled with an M. The panels were illuminated for 6 h with two 100 W, 380 nm water cooled LEDs; one experiment using 400 nm LEDs is also described. Every 6 min, the illumination was interrupted and a digital image of the hydrogen sensitive tape was recorded. At the conclusion, the maximum observable rates of hydrogen production were determined using the pressure-dependent logarithmic model described in reference [27]. Each measurement was repeated in the following way. After the initial 6 h, the reactor was disassembled in a well-ventilated fume hood to release the gas in the head space of the reactor. After allowing time for the gas to be replaced with air, fresh hydrogen sensitive tape was applied, the reactor was reassembled and the reaction was run under the same conditions. To estimate the uncertainty of

the measurements, each panel of catalysts included five vials containing the same material. The hydrogen evolution rates from these five vials was used to determine a mean and standard deviation and the uncertainty was reported as plus or minus one standard deviation.

2.6. Physical characterization of catalysts

A Quanta 200 (FEI) Scanning electron microscope (SEM) was used to image the shape and the size of all the core particles. Transmission electron microscopy (TEM) images of S310T were recorded using a Tecnai F20 TEM (FEI). The specific surface areas of catalysts were determined using Brunauer–Emmett–Teller (BET) method involving N₂ adsorption–desorption measurements (NOVA 2200E, Quantachrome, FL).

3. Results

Sixteen types of cores were used in this study and SEM images of each type are shown in Figs. S1 and S2. SEM images of 12 types of SrTiO₃ samples containing 0, 1, 2, or 3 wt % of added Al annealed in a SrCl₂ melt at 900, 1000, or 1100 °C are shown in Fig. S1. The SrTiO₃ particles annealed in SrCl₂ molten salts with no Al₂O₃ additions (S09, S010, and S011) are larger (0.5 to 2 μm) and have more polygonal shapes. The SrTiO₃ particles annealed in SrCl₂ with added Al₂O₃ are smaller (0.1-1 μm) and have irregular shapes. The appearance of the S011 particles is consistent with a previous report¹⁸ of SrTiO₃ prepared in the same way. Figure S2 shows SEM images of the SrTiO₃ samples that were doped by annealing in the solid state and then annealed in SrCl₂ at 1000 °C. These particles have irregular shapes and are 0.1-1 μm in diameter, similar to S110, S210, and S310 shown in Fig. S1.

The rates of hydrogen evolution from the core samples doped by adding Al₂O₃ to the molten salt were measured in a single array of the PAPCR, referred to as Array 1, during illumination

with 380 nm light. The catalysts and reaction conditions for each cell in Array 1 are provided in Table 1. Note that the spatial arrangement of the labels in Table 1 (and those that follow) is the same as the spatial arrangement of the individual vials in the array in the PAPCR and the Figures depicting hydrogen evolution. Images of Array 1 before and after the first and second run are illustrated in Fig. S3, where one can see that the hydrogen sensitive material above individual reactors darkened by different amounts. The change in darkness of each vile (the concentration of hydrogen in the vile) recorded as a function of time is shown in Fig.S4, and the hydrogen generation rates determined from these data are illustrated in Fig. 1. The results from the second run (Fig. S5) are consistent within the standard deviation of the measurements. However, we note that 16 of 20 vials with detectible concentrations of hydrogen produced more hydrogen in the second run than in the first run.

Table 1. Description and spatial arrangement of the contents of each reactor in Array 1

Sample, pH, Powder Mass/Volume of Solution (mg/ml)*										
S19,2	S29,2	S39,2	S010,2	S110,2	S210,2	S310,2	S011,2	S111,2	S211,2	S311,2
S19,6	S29,6	S39,6	S010,6	S110,6	S210,6	S310,6	S011,6	S111,6	S211,6	S311,6
S19,12	S29,12	S39,12	S010,12	S110,12	S210,12	S310,12	S011,12	S111,12	S211,12	S311,12
K19,2	K29,2	K39,2	K010,2	K110,2	K210,2	K310,2	K011,2	K111,2	K211,2	K311,2
K19,6	K29,6	K39,6	K010,6	K110,6	K210,6	K310,6	K011,6	K111,6	K211,6	K311,6
K19,12	K29,12	K39,12	K010,12	K110,12	K210,12	K310,12	K011,12	K111,12	K211,12	K311,12
K211,6P	K211,12P	S211,6	K211,2M	K211,6M	K211,12M	S211,6	none, 2	none, 6	none, 12	S211,6
S211,6, 1.6/0.4	S211,6, 0.8/0.4	S211,6, 0.4/0.4	S211,6	S211,6, 6.4/0.8	S211,6, 3.2/0.8	S211,6, 1.6/0.8	S211,6, 0.8/0.8	empty	empty	empty

*For those with only sample and pH parameters, the weight of powder/volume of solution (6.4 mg/0.4 ml) was omitted.

Notes for interpreting table entries:

First character: heated in S = SrCl₂ or K = KCl

Second character: wt % added Al₂O₃ as 0, 1, 2, or 3 wt %.

Third Character(s): °C heated at 9 = 900, 10 = 1000, or 11 = 1100

none = solution, but no catalyst

empty = no solution, no catalyst

M: 8 vol% methanol added to solution

P: Pt 1 wt% surface co-catalyst.

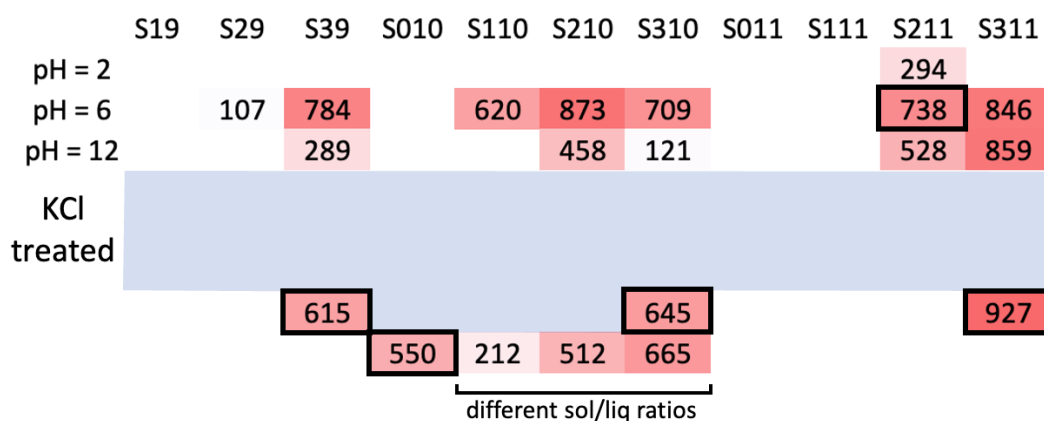


Figure 1. Mass specific rates of hydrogen production from Array 1 for the first run. Cells with no numbers did not produce hydrogen above the detectible limit. In other cells, the number has units of $\mu\text{mol}/(\text{g}\cdot\text{h})$. As a guide to the eye, each cell is colored from white to red such that the minimum value is white and the maximum value is the darkest red. Based on the five identical samples denoted by a black border (S211, pH6), the average \pm standard deviation is $695 \pm 146 \mu\text{mol}/(\text{g}\cdot\text{h})$.

When interpreting Fig. 1, note that cells without numbers produced hydrogen at a rate below the detectible limit. For a 6 h run and typical catalyst/liquid ratios in this reactor, the lower limit of hydrogen detection is approximately $100 \mu\text{mol}/\text{g}\cdot\text{h}$. In other words, this does not mean that these materials produce no H_2 , but that the rate of production is less than $100 \mu\text{mol}/\text{g}\cdot\text{h}$. None of the catalysts treated in molten KCl, whose cells are shaded but have no numbers in Fig. 1, produced hydrogen at a detectible rate. As controls, some cells had solution, but no catalyst (labeled none), and others were empty. As expected, none of these cells produced detectible H_2 . To estimate the uncertainty of the measurement, five of the vials were filled with an identical catalyst. The average and standard deviation of the measurements from these five reactors was $695 \pm 146 \mu\text{mol}/(\text{g}\cdot\text{h})$. Based on many experiments, typical uncertainty for the PAPCR range from 5 to 21 %.

The results in Fig. 1 show that Al-doped SrTiO_3 in water with pH 6 produces H_2 at a greater rate than pH 2. In most cases a solution of pH 6 is also better than pH 12, but for the sample

heated at 1100 °C, they are comparable. This is consistent with previous studies of the pH dependence of the photochemical reactivity of SrTiO₃, measured by the photo reduction of aqueous silver cations, which showed that reactivity increased with pH in the acidic range, reached a maximum in the range of 5-7, and then remained roughly constant until pH 12.²⁸

The results also indicate that the concentration of Al added to the SrCl₂ melt influences the reactivity. Samples with 2 wt % or 3 wt % added Al produced H₂ at greater rates than samples with 0 wt % or 1 wt %. To interpret these results, we emphasize that the variable controlled in this study was the amount of Al₂O₃ added to the melt – the amount of Al that dissolved into the SrTiO₃ was not measured. Previous measurements reported by Ham et al.¹⁸ found that SrTiO₃ treated in the same way at 900 °C, 1000 °C, and 1100 °C contained 0.12 %, 0.11 %, and 0.31 % Al. The increase in Al concentration at the higher temperature is not surprising, as both the rate of diffusion into SrTiO₃ and the solubility limit are likely to increase with temperature. The current results indicate that added Al₂O₃, up to at least 2 wt %, increases the rate of H₂ production. We note that even the samples with 0 wt % added Al₂O₃ contain some Al, as it is known that the alumina crucible also serves as an Al source.¹⁸ However, the results show that additionally added Al₂O₃ is beneficial to the rate of H₂ production.

The rates of hydrogen generation from the samples with Al added by annealing in the solid state were measured in Array 2 (See Table S1 for a description of the powders) and were mostly below the detectable limit; in all cases, the rates were less than the rates for the catalysts doped by adding Al₂O₃ to the SrCl₂ melt. For example, the hydrogen evolution rate from sample ss-S110 at pH 6 during the second run was 344 μmol/h/g, compared to 620 μmol/h/g for the comparable sample with Al₂O₃ added to the molten salt. Because the samples have similar surface areas and were treated similarly, we surmise that the solid-state method of Al-doping

employed here creates samples with Al-concentrations that are either less than or greater than the ideal concentration range.

With the rates of hydrogen evolution from the core materials established, high surface area sol-gel titania shells were added to the cores. TEM images of one of the titania coated catalysts (S310T) are provided in Fig. 2. The SrTiO_3 cores are not electron transparent and appear black in these images. However, at the edges of the particles, there is a clear layer of very fine-grained material supported by the opaque core. This is the titania shell and has the same morphological characteristics as described in earlier reports.^{11,13}

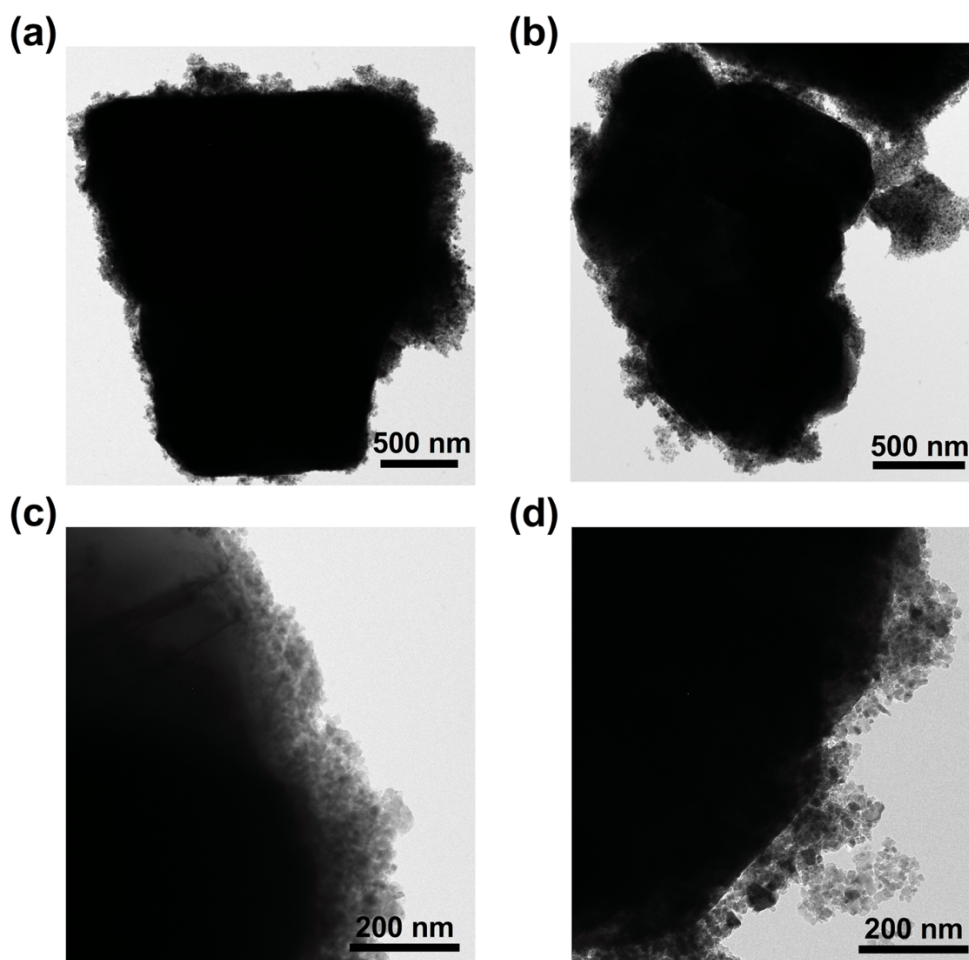


Figure 2. TEM images of S310T $\text{SrTiO}_3/\text{TiO}_2$ core/shell particles.

Array 3 was used to measure the hydrogen evolution rates from the TiO₂ coated Al-doped SrTiO₃ core/shell catalysts. The catalysts and their positions in the array are presented in Table 2. Images of Array 3 before and after the reaction are provided in Fig. S6 and the amount of hydrogen in each vial as a function of time is shown in Fig. S7. The rates of hydrogen evolution are shown in Fig. 3. When the experiment was repeated, the results were similar and are shown in Fig. S8. There is a dashed grey rectangle in Array 3 that marks the position of the cores doped by solid state annealing, all of which had rates below the detectible limit in the first run. This subset of Array 3 was previously referred to as Array 2. The five P25 samples used to estimate the uncertainty ($2271 \pm 36 \mu\text{mol}/(\text{g}\cdot\text{h})$) are surrounded by black rectangles.

Table 2. Description and spatial arrangement of the contents of each reactor in Array 3*

Powder, pH											
ss-S010, 2	ss-S110, 2	ss-S210, 2	ss-S310, 2	ss-S010T, 2M	ss-S110T, 2M	ss-S210T, 2M	ss-S310T, 2M	S010T, 2M	S110T, 2M	S210T, 2M	S310T, 2M
ss-S010, 6	ss-S110, 6	ss-S210, 6	ss-S310, 6	ss-S010T, 6M	ss-S110T, 6M	ss-S210T, 6M	ss-S310T, 6M	S010T, 6M	S110T, 6M	S210T, 6M	S310T, 6M
ss-S010, 9	ss-S110, 9	ss-S210, 9	ss-S310, 9	ss-S010T, 9M	ss-S110T, 9M	ss-S210T, 9M	ss-S310T, 9M	S010T, 9M	S110T, 9M	S210T, 9M	S310T, 9M
ss-S010, 12	ss-S110, 12	ss-S210, 12	ss-S310, 12	ss-S010T, 12M	ss-S110T, 12M	ss-S210T, 12M	ss-S310T, 12M	S010T, 12M	S110T, 12M	S210T, 12M	S310T, 12M
s,2M	s,6M	s,9M	s,12M	P25,6M	P25,6M	empty	empty	empty	empty	empty	empty
f,2M	f,6M	f,9M	f,12M	P25,6M	P25,6M	P25,6M	empty	empty	empty	empty	empty

*The weight of powder/volume of solution is 6.4 mg/0.4 ml for all suspensions. The prefix "ss-" denotes Al doping by solid state annealing. The parameter "f" denotes the use of faceted SrTiO₃ cores. All other nomenclature is described in the notes for Table 1.

	SS-S010	SS-S110	SS-S210	SS-S310	SS-S010T	SS-S110T	SS-S210T	SS-S310T	S010T	S110T	S210T	S310T
pH = 2						2267	2423	2236	2126	2415	2226	3458
pH = 6					1648	2280	2407	1741	2114	2843	2351	3805
pH = 9					2586	2836	2905	2190	2229	2899	2362	4345
pH = 12					2054	1810	2581	2011	2080	1750	2899	3163
shell					2229	2266	2275					
faceted		2663	2070	1510	2327	2256						
	pH 2	pH 6	pH 9	pH 12	P25							

Figure 3. Mass specific rates of hydrogen production from Array 3 for the first run. Cells with no numbers produces hydrogen at a rate less than the detectible limit. In other cells, the number has units $\mu\text{mol}/(\text{g}\cdot\text{h})$. As a guide to the eye, each cell is colored from white to red such that the minimum value is white and the maximum value is the darkest red. Based on the five identical samples (platinized P25 TiO_2), the average \pm standard deviation is $2271 \pm 36 \mu\text{mol}/(\text{g}\cdot\text{h})$.

The results for the TiO_2 coated Al-doped SrTiO_3 core/shell catalysts doped by solid state annealing show a dependence both on the pH and on the amount of added Al_2O_3 . For all amounts of added Al, the maximum hydrogen yield occurs at pH 9. With one exception (S210T), this is also true for the samples doped in SrCl_2 . At all four pH values, the maximum rate of hydrogen production for the solid state doped samples occurs for samples annealed with 2 wt % Al; for the samples doped in SrCl_2 , the maximum is at 3 wt % Al. So, as for the bare cores in Array 1, we conclude that increased added Al leads to increased hydrogen production. The hydrogen yield from the core-shell catalysts with cores doped by solid state annealing is generally less than the comparable catalyst doped in SrCl_2 , with S210T being the exception. This trend mimics the behavior of the cores themselves.

A noteworthy difference between the testing of the cores and the core-shell catalyst is that methanol was added to the liquid as a sacrificial oxidant for the core-shell materials, to increase

the hydrogen yield to meaningful levels. It is, therefore, not possible to directly compare the reactivity of the cores by themselves to the core-shell catalysts. In addition to the presence of methanol, the two types of catalysts also require different co-catalysts. It should also be noted that, by design, the core shell materials have a much larger surface area (see Table 3).

Nevertheless, some core materials with low surface area, to which 8 vol% methanol was added as a sacrificial oxidant, had reactivities similar to those with the high surface area shells. These materials were obtained from the authors of reference [22], in which they are denoted C-Al. The faceted particles were hydrothermally synthesized, are bounded by {100} and {110} facets, and were annealed in SrCl₂ with 1 wt% Al₂O₃ at 1150 °C. With the addition of methanol, the Al-doped SrTiO₃ cores also have increased hydrogen yield and are comparable to most of the core-shell catalysts, even though there is no shell. Overall, the data indicate that the trends in performance of the core-shell catalysts with doping, temperature, and pH parallels the trends of the cores. Further, while the titania coating might enhance long term stability and improve the performance of the lowest reactivity cores (such as those produced by solid state doping), it does not contribute significantly to the hydrogen yield from the best cores. It should also be noted that among the catalysts with higher surface area shells, the reactivity in Fig. 3 does not strongly correlate with the surface areas in Table 3.

Table 3. The mass specific surface area of selected samples.

Sample	Mass specific surface area, m ² /g
S010	1
S310	1
S010T	16
S110T	40
S210T	27
S310T	33
s	1
P25	50

To determine the performance of the catalyst in visible light we replaced the 380 nm LED light source with a 400 nm LED source and illuminated the catalysts in Array 3. Because of the different illumination, we refer to this as array 4 (the contents are described in Table 2). To produce detectable amounts of hydrogen, the illumination was continued for 16.5 h. Because the accumulation of hydrogen in the head space of the reactor is integral, longer runs have the effect of making the minimum detectable rate smaller, making it possible to study catalysts that do not produce hydrogen at rates greater than 100 $\mu\text{mol}/(\text{g}\cdot\text{h})$. For this experiment, the minimum detectable rate is approximately 40 $\mu\text{mol}/(\text{g}\cdot\text{h})$. Images of the reactor before and after the 16.5 h illumination are illustrated in Fig. S9 and the amount of hydrogen as a function of time in each cell is shown in Fig. S10. The hydrogen evolution rates determined from these data are illustrated in Fig. 4. Most of the core-shell catalysts at pH 6 and pH 9 produced detectable hydrogen, but unlike the observations at 380 nm, they do not produce as much hydrogen as P25.

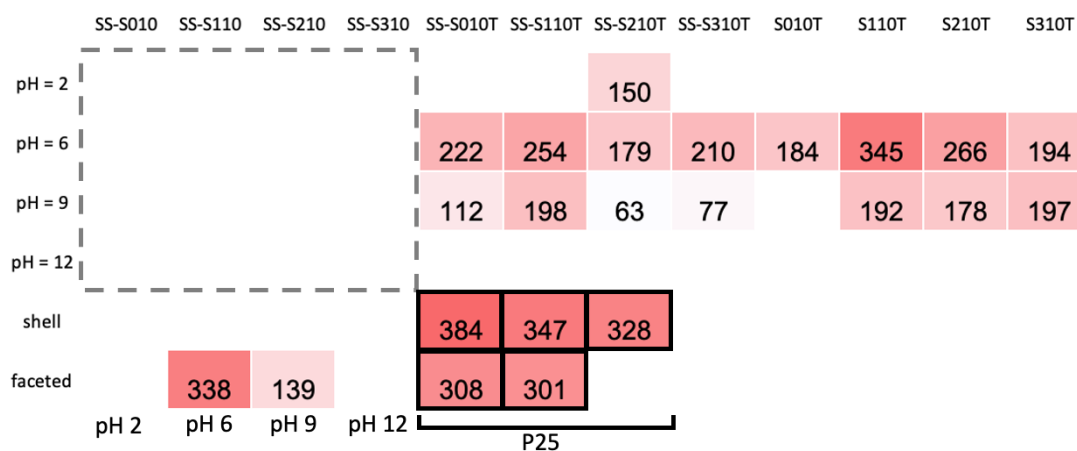


Figure 4. Mass specific rates of hydrogen production from Array 4 while illuminated with 400 nm light. Cells with no numbers did not produce hydrogen above the detectable limit. In other cells, the units are $\mu\text{mol}/(\text{g}\cdot\text{h})$. As a guide to the eye, each cell is colored from white to red such that the minimum value is white and the maximum value is the darkest red. Based on the five identical samples (platinized P25 TiO_2), the average \pm standard deviation is $334 \pm 33 \mu\text{mol}/(\text{g}\cdot\text{h})$.

4. Discussion

The SrTiO₃ cores treated in KCl yielded insignificant amounts of hydrogen compared to cores treated in SrCl₂. This is inconsistent with results reported by Kato et al.²⁹, who reported that among SrTiO₃ samples heated in molten LiCl, NaCl, KCl, and SrCl₂ at 1000 °C for 5 h in alumina crucibles, those heated in KCl yielded the most hydrogen and those heated in SrCl₂ yielded the least. In that previous work, aluminum was not deliberately added, but it is now known that the alumina crucible serves as an alumina source.¹⁸ The one significant difference between the current work and that reported by Kato et al.²⁹ is the fraction of salt added to the SrTiO₃, which was only 20 wt % rather than the 10 times excess used here. While we did not investigate this parameter, one can hypothesize that this is the source of the difference.

The Al-doped SrTiO₃ cores produce the most hydrogen if the Al is added during the molten salt treatment, if at least 2 wt % is added, and the molten salt treatment is carried out at 1000 °C or 1100 °C. That more Al added to the salt and a higher temperature increases performance suggest that the greater hydrogen yield is linked to an increase in the Al concentration in the bulk, as both of these factors promote Al incorporation and transport. Attempts to dope SrTiO₃ with Al by solid state annealing did not lead to catalysts with comparable activities. This suggests that Al incorporation is slower in the solid state than in the molten SrCl₂. In the former case, the Al is presumably in the form of an oxide while in the latter case, there might be free aluminum cations in the molten salt, and the substitution of such cations into the SrTiO₃ lattice might be more facile, as molten salts are known to facilitate ion exchange reactions.^{6,30} The cores were also more active in neutral and weakly alkaline solutions, consistent with earlier studies.^{22,28} As expected, the performance of the core-shell catalysts diminished significantly in

visible light (400 nm). In these conditions, hydrogen generation rates were comparable to or slightly less than from P25.

The relative hydrogen yield from the core-shell materials roughly parallels the performance of the cores. This indicates that the core has a significant influence on the performance of the core-shell material, and is not simply a support for the shell. This makes sense when one considers the source of the photogenerated carriers. The absorption coefficient of anatase³¹ is $1 \times 10^2 \text{ cm}^{-1}$ at 380 nm and the anatase thickness is approximately $1 \times 10^{-5} \text{ cm}$, meaning that it absorbs less than 1 % of the light. The absorption coefficient of the SrTiO₃ core³², on the other hand, is $3 \times 10^4 \text{ cm}^{-1}$ so most of the light will be absorbed by a core with dimensions on the order of $1 \times 10^{-4} \text{ cm}$. This means that the overwhelming majority of the photogenerated electrons and holes that participate in the reaction originate from the core and must be transported through the interface to the shell surface. Therefore, charge separation in the core and transport through the SrTiO₃/TiO₂ interface are important to the function of the catalyst.

The results here point to the importance of Al-doping in the SrTiO₃ core and it is the consensus of earlier studies that an increased Al concentration leads to greater yields of hydrogen.^{19,33} Unfortunately, there is sparse information about the solubility of Al in SrTiO₃. It has been reported that as much as 1.8 atomic % has been dissolved in SrTiO₃ at 1520 °C.³⁴ Wang et al.³⁵ recently provided evidence based on X-ray lattice parameters that the solubility limit is between 2 and 4 atomic % for samples heated at 1150 °C. Zhang³⁶ reported that SrTiO₃ heated for 10 h in SrCl₂ at 1150 °C in an alumina crucible had 2.6 atomic % Al, measured by ICP-OES. Yamakata et al.³³ reported Al concentrations in SrTiO₃ up to 0.31 % after heating for 10 h at 1100 °C in SrCl₂ in an alumina crucible. Equivalent results for the same conditions were reported by Ham et al.¹⁸ and Goto et al.¹⁷ reported Al concentrations of about 1 % in SrTiO₃

heated for 10 h at 1150 °C in and alumina crucible with SrCl₂, all measured by ICP-OES. Zhao et al.²⁰ reported concentrations as high as 7.8 % in hydrothermally synthesized Al-SrTiO₃. These concentrations were measured by X-ray fluorescence spectroscopy of powders. As an aliovalent dopant, such concentrations seem high, but the low temperature hydrothermal synthesis might trap non-equilibrium amounts of Al that cannot be sustained at higher temperature. Comparing the published results^{17,18,33} with from those in our lab,^{22,23,36} we find significant scatter (between 0.3 and 2.6 atomic % for similarly treated samples) and conclude that the uncertainty is comparable to the true concentration. Therefore, we must assume the Al concentrations are in the 0.3 to 2.6 atomic % range and increase with the concentration of Al added to the SrCl₂ melt, up to an as yet unknown solubility limit.

Aluminum doping is thought to improve the properties of SrTiO₃ by compensating pre-existing defects. In the undoped state, pre-existing oxygen vacancies are charge compensated by electrons according to the charge balance $2[V_O^{\bullet\bullet}] \approx n$.^{34,37} Some of these electrons are thought to be trapped at lattice Ti, leading to defects of the type Ti'_{Ti} , which act as recombination centers and decrease minority carrier lifetimes.¹⁹ Considering these defects, the electroneutrality condition in the undoped case is $2[V_O^{\bullet\bullet}] \approx n + [Ti'_{Ti}]$. The acceptor doping of Al shifts the electroneutrality to $2[V_O^{\bullet\bullet}] \approx [Al'_{Ti}]$,³⁷ which reduces the concentration of the Ti'_{Ti} recombination centers and ionized electrons, n . For an n-type semiconductor with bands bent in depletion, the width of the space charge region is inversely proportional to the square root of the donor density, n . Therefore, reducing the donor density also increases the width of the space charge region, as illustrated schematically in Fig. 5. Photogenerated charge carriers in the space charge region have the possibility of being separated, while those generated in the flat band region are likely to recombine. Increasing the size of the space charge region and reducing the concentration of

recombination centers act together to increase the number of photogenerated carriers that make it to the surface and can participate in the reaction. This is consistent with a previous report that Al-doping increases the carrier lifetimes in SrTiO₃ by more than two orders of magnitude.³⁸ Therefore, the observed variations in reactivity likely arise from different levels of defect compensation by Al, which alters the width of the space charge region. This is consistent with the results in Fig. 3, which show that the core-shell catalysts with the greatest amount of Al added to the SrCl₂ salt have the greatest reactivity.

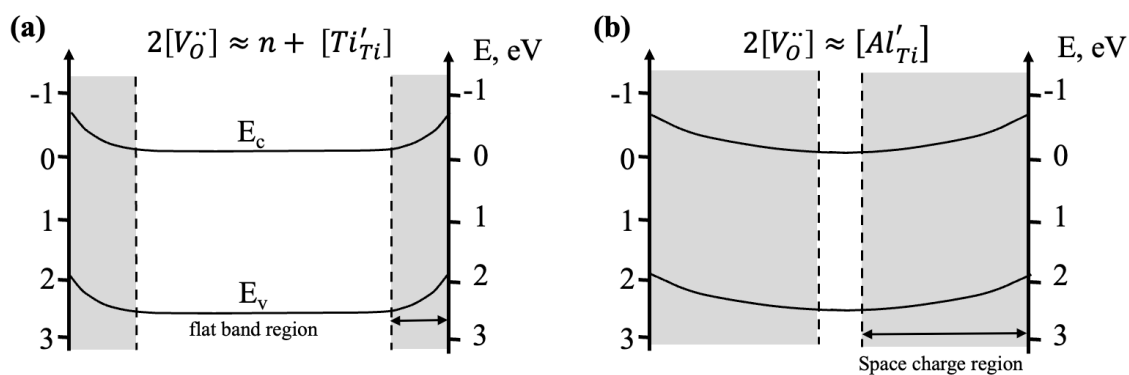


Figure 5. Schematic illustration of the space charge region below the surface of a SrTiO₃ core particle in the (a) undoped and (b) Al doped case. The compensation of oxygen vacancies by Al reduces the donor concentration and increases the width of the space charge.

As mentioned earlier, it is not possible to directly compare the reactivity of the cores themselves to the core-shell catalysts because of the difference in the conditions of the reaction (co-catalyst and methanol addition). While the core-shell catalysts in many cases produce more hydrogen than the cores by themselves, as illustrated by the solid-state doped materials, one must keep in mind that the addition of a sacrificial oxidant almost always leads to increased hydrogen production. When the best core materials are tested with methanol, the hydrogen yield does not differ significantly from comparable core-shell catalysts (Fig. 3). Despite the inability to compare the absolute rates of hydrogen production from the core and core-shell catalysts, it is possible to

compare the trends with processing parameters. This leads to the main finding of this paper, that the properties of the core-shell catalysts strongly depend on the characteristics of the core. The dependence of the hydrogen yield on Al-doping, temperature, and pH was similar in the cores and the core-shell catalysts. Rather than simply being a support for the higher surface area shell, the core performs the light harvesting function and the properties of the core-shell structure then hinge on its ability to separate photogenerated charge and increase carrier lifetime. While the shell can perform an important function by protecting the core from photo-corrosion, it does not necessarily contribute to the overall reactivity of the best core materials. This is consistent with model studies of the photochemical reactivity of titania supported on planar SrTiO₃ substrates, which showed that the reactivity of the titania overlayer closely mimics that of the SrTiO₃ substrate.³⁹ However, the findings contradict the view³ that the core-shell structure by itself can enhance reactivity.

Al-doped SrTiO₃ is among the most efficient water splitting catalysts known,²¹ but is ultimately limited in performance by the size of its bandgap compared to the solar spectrum. The challenge for the future is take what has been learned about controlling particle shape, charge separation, and defect compensation that makes Al-doped SrTiO₃ an efficient catalyst and apply this to a material that absorbs more of the solar spectrum. While materials with smaller bandgaps tend to photo-corrode in the reaction conditions, the current results suggest that TiO₂ coatings might be used to stabilize them.

5. Conclusion

The rate of hydrogen generation from various Al-doped SrTiO₃/TiO₂ core-shell photocatalysts studied here varies by a factor of more than 40 based on variations in the core characteristics. Catalysts with cores treated in molten KCl did not yield significant amounts of

hydrogen. The hydrogen generation rates from the core-shell catalysts varied in the same way as the hydrogen generation rates from the core. The best catalysts had 2 or 3 mole percent added Al, incorporated in the SrTiO₃ during treatment in a SrCl₂ molten salt at 1000 °C or 1100 °C. The hydrogen generation rates from the best catalysts exceeded that of P25 titania when irradiated with 380 nm light. The core component of the catalyst is where the vast majority of the photogenerated electron-hole pairs are generated. Because to this, the core's ability to separate the charge carriers, prevent recombination, and transport them to the surface is beneficial to the overall properties of the core-shell catalyst. While the shell is less effective in determining the reactivity of the catalyst, it can still serve to protect the core from degradation.

Acknowledgements

This work was supported by the National Science Foundation under Grant Number: DMR 2016267, and the authors acknowledge the use of the Materials Characterization Facility at Carnegie Mellon University supported by Grant Number: MCF-677785.

Appendix A. Supplementary Material

Supplementary material related to this article is provided.

References Cited

- ¹Tao, X. P., Zhao, Y., Wang, S. Y., Li, C., and Li, R. G., Recent advances and perspectives for solar-driven water splitting using particulate photocatalysts, *Chem Soc Rev.* 2022;51(9):3561-608.
- ²Wang, Z., Li, C., and Domen, K., Recent developments in heterogeneous photocatalysts for solar-driven overall water splitting, *Chem Soc Rev.* 2019;48(7):2109-25.
- ³Rao, V. N., Reddy, N. L., Preethi, V., Karthik, M., Yu, Y. T., Yang, J. M., Kumari, M. M., and Shankar, M. V., A critical review on core/shell-based nanostructured photocatalysts for improved hydrogen generation, *Int J hydrogen Energy.* 2023;48(31):11754-74.

- ⁴Ullah, S., Ferreira-Neto, E. P., Khan, A. A., Medeiros, I. P. M., and Wender, H., Supported nanostructured photocatalysts: the role of support-photocatalyst interactions, *Photochem Photobiol Sci.* 2023;22(1):219-40.
- ⁵Weng, B., Qi, M. Y., Han, C., Tang, Z. R., and Xu, Y. J., Photocorrosion Inhibition of Semiconductor-Based Photocatalysts: Basic Principle, Current Development, and Future Perspective, *ACS Catal.* 2019;9(5):4642-87.
- ⁶Luo, L. Y., Wang, S. Y., Wang, H., Tian, C. G., and Jiang, B. J., Molten-Salt Technology Application for the Synthesis of Photocatalytic Materials, *Energy Tech.* 2021;9(2):
- ⁷Wu, J., Ke, K. H., Qin, N., Lin, E. Z., Kang, Z. H., and Bao, D. H., Magnetically retrievable Fe₃O₄@SiO₂@ZnO piezo-photocatalyst: Synthesis and multiple catalytic properties, *J Colloid Interface Sci.* 2023;636(167-75).
- ⁸Zhang, J., Bang, J. H., Tang, C., and Kamat, P. V., Tailored TiO₂-SrTiO₃ Heterostructure Nanotube Arrays for Improved Photoelectrochemical Performance, *ACS Nano.* 2010;4(1):387-95.
- ⁹Zhao, H., Li, C. F., Liu, L. Y., Palma, B., Hu, Z. Y., Rennekar, S., Larter, S., Li, Y., Kibria, M. G., Hu, J. G., and Su, B. L., n-p Heterojunction of TiO₂-NiO core-shell structure for efficient hydrogen generation and lignin photoreforming, *J Colloid Interface Sci.* 2021;585(694-704).
- ¹⁰Hu, H. Y., Lin, Y., and Hu, Y. H., Synthesis, structures and applications of single component core-shell structured TiO₂: A review, *Chem Eng J.* 2019;375(
- ¹¹Li, L., Rohrer, G. S., and Salvador, P. A., Heterostructured Ceramic Powders for Photocatalytic Hydrogen Production: Nanostructured TiO₂ Shells Surrounding Microcrystalline (Ba,Sr)TiO₃ Cores, *J. Am. Ceram. Soc.* 2012;95(4):1414-20.
- ¹²Li, L., Zhang, Y. L., Schultz, A. M., Liu, X., Salvador, P. A., and Rohrer, G. S., Visible light photochemical activity of heterostructured PbTiO₃-TiO₂ core-shell particles, *Catal. Sci. Technol.* 2012;2(9):1945-52.
- ¹³Li, L., Liu, X., Zhang, Y. L., Salvador, P. A., and Rohrer, G. S., Heterostructured (Ba,Sr)TiO₃/TiO₂ core/shell photocatalysts: Influence of processing and structure on hydrogen production, *International Journal of Hydrogen Energy.* 2013;38(17):6948-59.
- ¹⁴Yeredla, R. R., and Xu, H., Incorporating strong polarity minerals of tourmaline with semiconductor titania to improve the photosplitting of water, *J Phys Chem C.* 2008;112(2):532-39.
- ¹⁵Gao, B., Kim, Y. J., Chakraborty, A. K., and Lee, W. I., Efficient decomposition of organic compounds with FeTiO₃/TiO₂ heterojunction under visible light irradiation, *Appl Catal B.* 2008;83(3-4):202-07.
- ¹⁶Li, L., Liu, X., Zhang, Y. L., Nuhfer, N. T., Barmak, K., Salvador, P. A., and Rohrer, G. S., Visible-Light Photochemical Activity of Heterostructured Core-Shell Materials Composed of Selected Ternary Titanates and Ferrites Coated by TiO₂, *ACS Appl Mater Interfaces.* 2013;5(11):5064-71.
- ¹⁷Goto, Y., Hisatomi, T., Wang, Q., Higashi, T., Ishikiriyama, K., Maeda, T., Sakata, Y., Okunaka, S., Tokudome, H., Katayama, M., Akiyama, S., Nishiyama, H., Inoue, Y., Takewaki, T., Setoyama, T., Minegishi, T., Takata, T., Yamada, T., and Domen, K., A Particulate Photocatalyst Water-Splitting Panel for Large-Scale Solar Hydrogen Generation, *Joule.* 2018;2(3):509-20.

- ¹⁸Ham, Y., Hisatomi, T., Goto, Y., Moriya, Y., Sakata, Y., Yamakata, A., Kubota, J., and Domen, K., Flux-mediated doping of SrTiO₃ photocatalysts for efficient overall water splitting, *J Mater Chem A*. 2016;4(8):3027-33.
- ¹⁹Zhao, Z., Goncalves, R. V., Barman, S. K., Willard, E. J., Byle, E., Perry, R., Wu, Z., Huda, M. N., Moulé, A. J., and Osterloh, F. E., Electronic structure basis for enhanced overall water splitting photocatalysis with aluminum doped SrTiO₃ in natural sunlight, *Energy Environ Sci*. 2019;12(4):1385-95.
- ²⁰Zhao, Z. Q., Willard, E. J., Li, H., Wu, Z. K., Castro, R. H. R., and Osterloh, F. E., Aluminum enhances photochemical charge separation in strontium titanate nanocrystal photocatalysts for overall water splitting, *J Mater Chem A*. 2018;6(33):16170-76.
- ²¹Takata, T., Jiang, J., Sakata, Y., Nakabayashi, M., Shibata, N., Nandal, V., Seki, K., Hisatomi, T., and Domen, K., Photocatalytic water splitting with a quantum efficiency of almost unity, *Nature*. 2020;581(7809):411-14.
- ²²Zhang, M. Y., Salvador, P. A., and Rohrer, G. S., Influence of particle size and shape on the rate of hydrogen produced by Al-doped SrTiO₃ photocatalysts, *J Am Ceram Soc*. 2022;105(8):5336-46.
- ²³Zhang, M. Y., Lopato, E. M., Ene, N. N., Funni, S. D., Du, T. X., Jiang, K. Y., Bernhard, S., Salvador, P. A., and Rohrer, G. S., Synthesis and Structure of an Ion-Exchanged SrTiO₃ Photocatalyst with Improved Reactivity for Hydrogen Evolution, *Adv Mater Interfaces*. 2023;10(10):
- ²⁴Maeda, K., Teramura, K., Lu, D. L., Takata, T., Saito, N., Inoue, Y., and Domen, K., Characterization of Rh-Cr mixed-oxide nanoparticles dispersed on (Ga_{1-x}Zn_x)(N_{1-x}O_x) as a cocatalyst for visible-light-driven overall water splitting, *J Phys Chem B*. 2006;110(28):13753-58.
- ²⁵Vorontsov, A. V., Stoyanova, I. V., Kozlov, D. V., Simagina, V. I., and Savinov, E. N., Kinetics of the photocatalytic oxidation of gaseous acetone over platinumized titanium dioxide, *Journal of Catalysis*. 2000;189(2):360-69.
- ²⁶Lopato, E. M., Eikey, E. A., Simon, Z. C., Back, S., Tran, K., Lewis, J., Kowalewski, J. F., Yazdi, S., Kitchin, J. R., Ulissi, Z. W., Millstone, J. E., and Bernhard, S., Parallelized Screening of Characterized and DFT-Modeled Bimetallic Colloidal Cocatalysts for Photocatalytic Hydrogen Evolution, *ACS Catal*. 2020;10(7):4244-52.
- ²⁷Song, W. J., Lopato, E. M., Bernhard, S., Salvador, P. A., and Rohrer, G. S., High-throughput measurement of the influence of pH on hydrogen production from BaTiO₃/TiO₂ core/shell photocatalysts, *Applied Catalysis B-Environmental*. 2020;269(
- ²⁸Zhang, M. Y., Salvador, P. A., and Rohrer, G. S., Influence of pH and Surface Orientation on the Photochemical Reactivity of SrTiO₃, *ACS Appl Energy Mater*. 2020;12(20):23617-26.
- ²⁹Kobayashi, M., Hara, M., and Kakihana, M., Fabrication of SrTiO₃ exposing characteristic facets using molten salt flux and improvement of photocatalytic activity for water splitting, *Catal Sci Technol*. 2013;3(7):1733-38.
- ³⁰Gabilondo, E., O'Donnell, S., Newell, R., Broughton, R., Mateus, M., Jones, J. L., and Maggard, P. A., Renaissance of Topotactic Ion-Exchange for Functional Solids with Close Packed Structures, *Chem Eur J*. 2022;28(33):
- ³¹Tang, H., Levy, F., Berger, H., and Schmid, P. E., Urbach Tail of Anatase TiO₂, *Phys. Rev. B*. 1995;52(11):7771-74.

- ³²Frye, A., French, R. H., and Bonnell, D. A., Optical properties and electronic structure of oxidized and reduced single-crystal strontium titanate, *Z. Metal.* 2003;94(3):226-32.
- ³³Yamakata, A., Yeilin, H., Kawaguchi, M., Hisatomi, T., Kubota, J., Sakata, Y., and Domen, K., Morphology-sensitive trapping states of photogenerated charge carriers on SrTiO₃ particles studied by time-resolved visible to Mid-IR absorption spectroscopy: The effects of molten salt flux treatments, *J. Photochem. Photobiol. A.* 2015;313(168-75).
- ³⁴Shin, C. J., Yoo, H. I., and Lee, C. E., Al-doped SrTiO₃: Part I, anomalous oxygen nonstoichiometry, *Solid State Ionics.* 2007;178(15-18):1081-87.
- ³⁵Wang, S. Y., Teramura, K., Hisatomi, T., Domen, K., Asakura, H., Hosokawa, S., and Tanaka, T., Effective Driving of Ag-Loaded and Al-Doped SrTiO₃ under Irradiation at $\lambda > 300$ nm for the Photocatalytic Conversion of CO₂ by H₂O, *ACS APPLIED ENERGY MATERIALS.* 2020;3(2):1468-75.
- ³⁶Zhang, M., "Enhancing Charge Separation on Metal Oxides by Space Charge Engineering for Photocatalytic Overall Water Splitting." in *Materials Science and Engineering*, **Vol. Ph.D.** Carnegie Mellon University, 2022.
- ³⁷Chan, N. H., Sharma, R. K., and Smyth, D. M., Non-stoichiometry in SrTiO₃, *J Electrochem Soc.* 1981;128(8):1762-69.
- ³⁸Murthy, D. H. K., Nandal, V., Furube, A., Seki, K., Katoh, R., Lyu, H., Hisatomi, T., Domen, K., and Matsuzaki, H., Origin of Enhanced Overall Water Splitting Efficiency in Aluminum-Doped SrTiO₃ Photocatalyst, *Adv. Energy Mater.* 2023;13(40):2302064.
- ³⁹Zhu, Y. S., Salvador, P. A., and Rohrer, G. S., Buried Charge at the TiO₂/SrTiO₃ (111) Interface and Its Effect on Photochemical Reactivity, *ACS Appl. Mater. Interfaces.* 2017;9(8):7843-51.

**Supplementary Materials for:
Influence of Al-doped SrTiO₃ cores on hydrogen evolution from SrTiO₃/TiO₂ core-shell catalysts**

Wenjia Song, Paul A. Salvador, and Gregory S. Rohrer*

Department of Materials Science and Engineering, Carnegie Mellon University, Pittsburgh, Pennsylvania 15213, United States.

*Corresponding author: E-mail: gr20@andrew.cmu.edu

This supplemental materials section contains supporting data on the particle morphologies and the hydrogen evolution experiments. The data for each array of catalysts involves images of the array before and after the reaction, kinetic data showing the hydrogen content in each reactor as a function of time, and a repeated experimental sequence to test for reproducibility. The data are included in this section while the summary results are in the main body of the paper. An inventory of the data in this document follows.

X-ray diffraction pattern of sol-gel synthesized titania	S1
Images of the core particles:	S2 and S3
Images of array 1, 3, and 4	S4, S7, S10
Hydrogen yield versus time for array 1, 3, and 4	S5, S8, S11
Results from the second run of array 1 and 3	S6, S9

1. Diffraction pattern of sol-gel titania coating

An X-ray diffraction pattern of the sol-gel produced titania coating is shown in Fig. S1. The diffraction pattern shows a mixture of anatase and rutile and is more than 90 % anatase. The peak widths indicate an average crystal size of 14 nm.

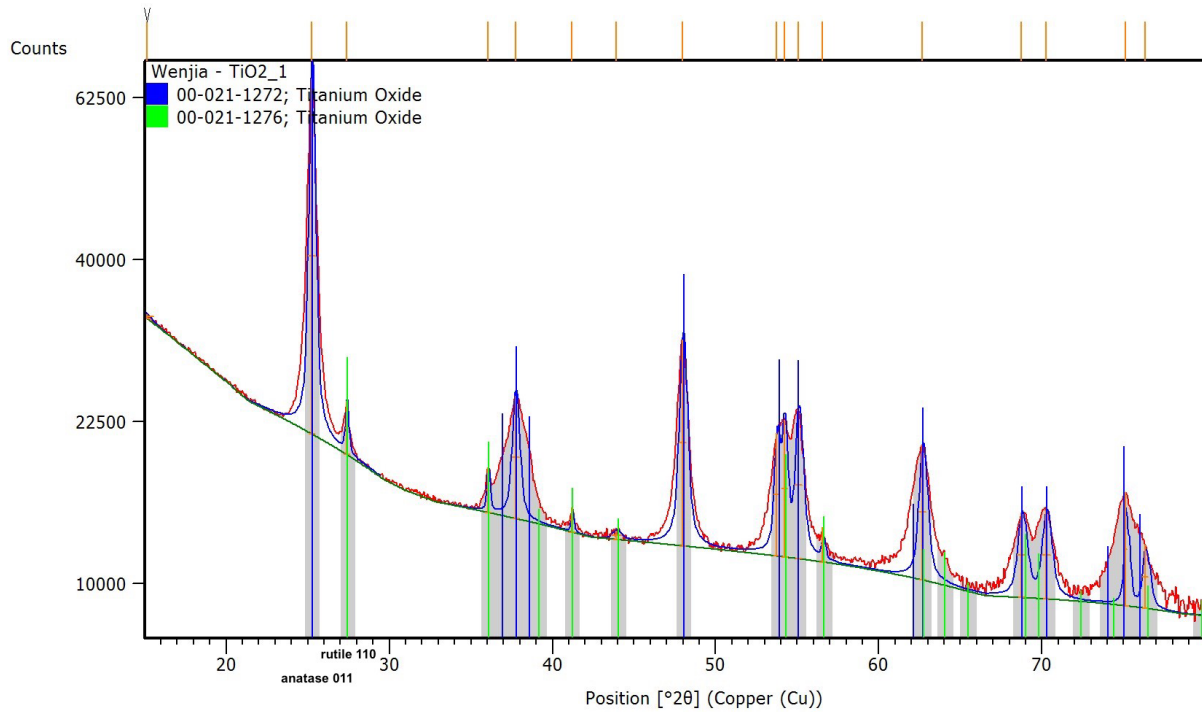


Figure S1. X-ray powder diffraction pattern of sol-gel produced titania recorded with Cu K_{α} radiation. Blue marks diffraction peaks from anatase and green marks those from rutile.

2. Particle morphologies

Figure S2 shows the SEM images of SrTiO_3 samples containing 0, 1, 2, or 3 wt % of added Al annealed in a SrCl_2 melt at 900, 1000, or 1100 °C. The dimensions of the field of view in all images is the same. Figure S3 shows SEM images of the SrTiO_3 samples that were doped by annealing in the solid state and then annealed in SrCl_2 at 1000 °C. The dimensions of the field of view in all images is the same.

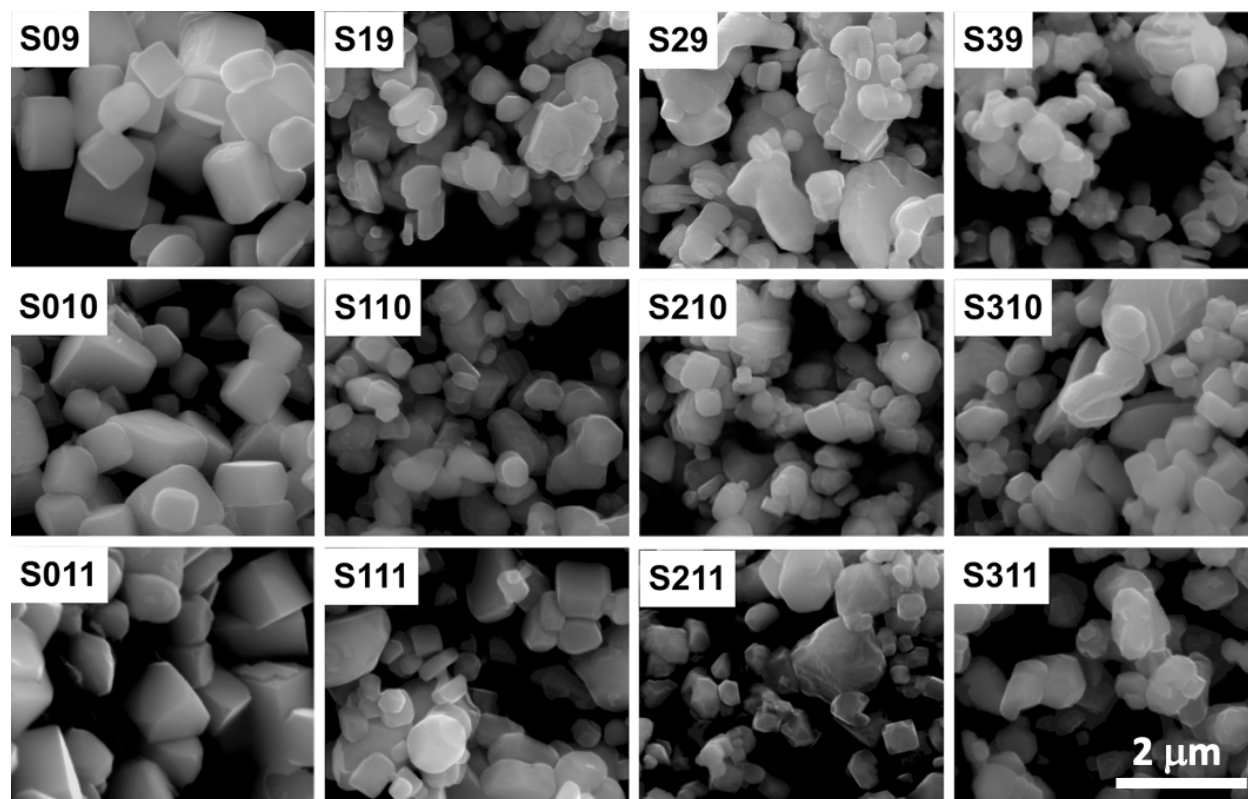


Figure S2. SEM images of SrTiO₃ samples doped at different temperatures by adding different amounts of Al₂O₃ to the SrCl₂ melt. The images have the same scale, quantified by the scale marker in the image of sample S311.

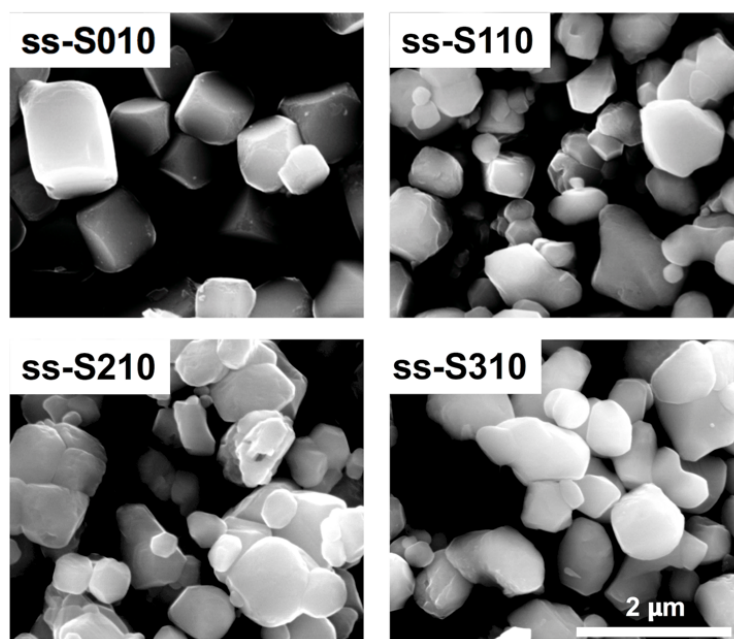


Figure S3. SEM images of SrTiO₃ samples doped with Al by annealing in the solid state. Each image shows the same field of view and the scale is quantified by the bar in the image of ss-S310.

3. Data from the hydrogen evolution experiments

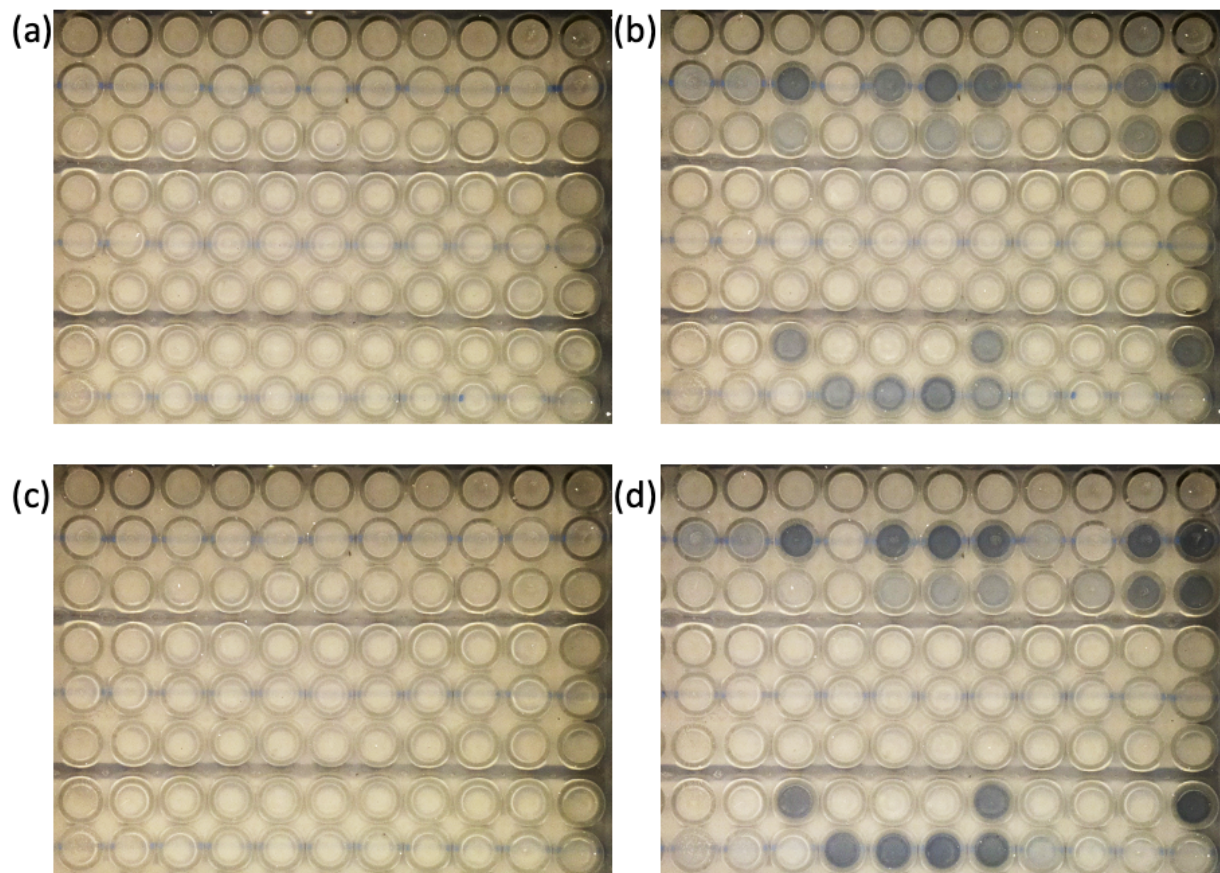


Figure S4. The pictures of reactor Array 1. The contents are described in Table 1. (a) before and (b) after the first 6 h run. The image looks down on the hydrogen sensitive tape. Each circle is the top of one of the glass vial reactors. The intensity of the color change is related to the hydrogen concentration. (c) before and (d) after the second 6 h run.

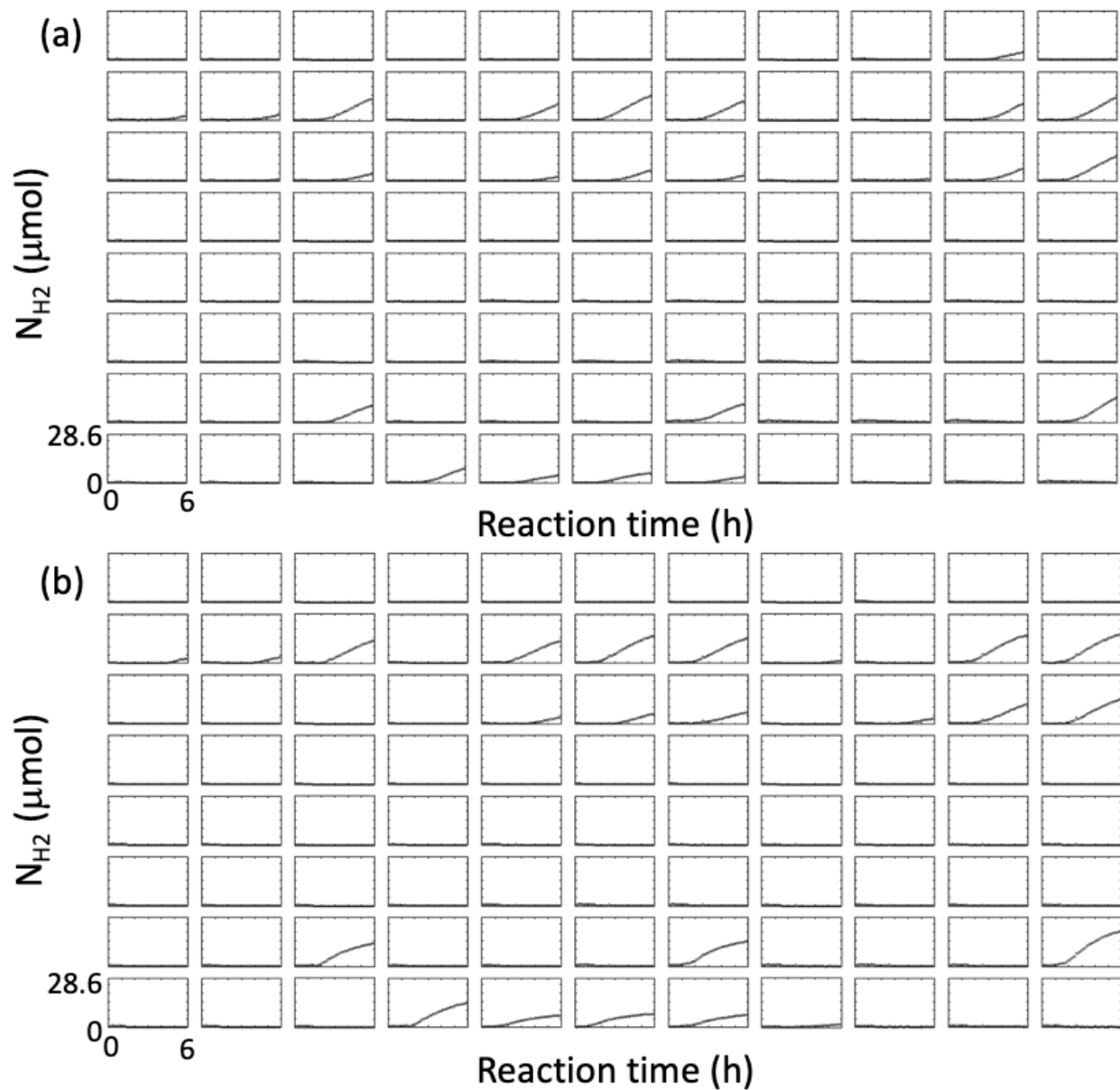


Figure S5. The amount of hydrogen in each vial of reactor Array 1. Each rectangle represents one of the vials in Fig. S2 and the contents are described in Table 1. Each graph has a domain of 0 to 6 h on the horizontal axis and 0 to 28.6 μmol hydrogen on the vertical axis. (a) First 6 h reaction. (b) Second 6 h reaction.

	S19	S29	S39	S010	S110	S210	S310	S011	S111	S211	S311
pH = 2											
pH = 6		263	775		745	930	828			969	995
pH = 12					287	397	376			688	827
			770				874				1295
				809	286	711	1243				

Figure S6. Mass specific rates of hydrogen production from Array 1 for the second run. Cells with no numbers did not produce hydrogen above the detectible limit. In other cells, the number has units $\mu\text{mol}/(\text{g}\cdot\text{h})$. As a guide to the eye, each cell is colored from white to red such that the minimum value is white and the maximum value is the darked red. Based on the five identical samples, the average value \pm standard deviation is $943 \pm 211 \mu\text{mol}/(\text{g}\cdot\text{h})$.

Table S1. Description and spatial arrangement of the contents of each reactor in Array 2*

Powder, pH			
ss-S010, 2	ss-S110, 2	ss-S210, 2	ss-S310, 2
ss-S010, 6	ss-S110, 6	ss-S210, 6	ss-S310, 6
ss-S010, 9	ss-S110, 9	ss-S210, 9	ss-S310, 9
ss-S010, 12	ss-S110, 12	ss-S210, 12	ss-S310, 12

*The nomenclature used to designate the different experiments is explained in the notes to Table 1.

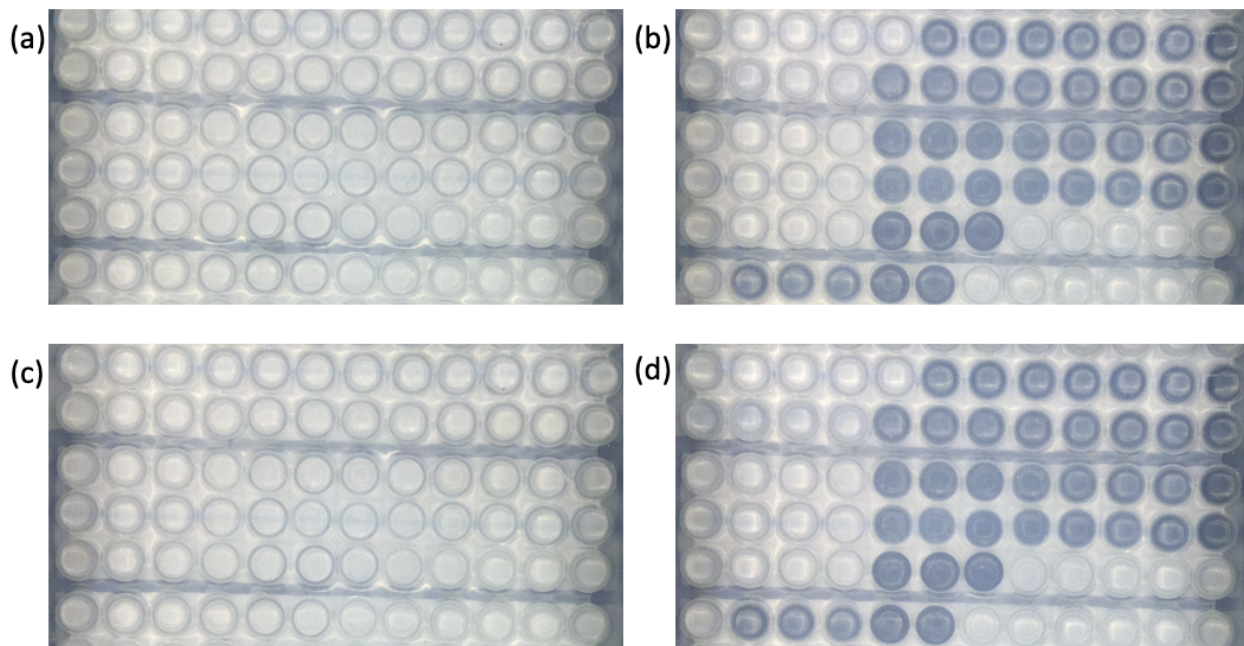


Figure S7. The pictures of reactor Array 3 (a) before and (b) after the first 6 h run. The contents are described in Table 2. The image looks down on the hydrogen sensitive tape. The intensity of the color change is related to the hydrogen concentration. (c) before and (d) after the second 6 h run.

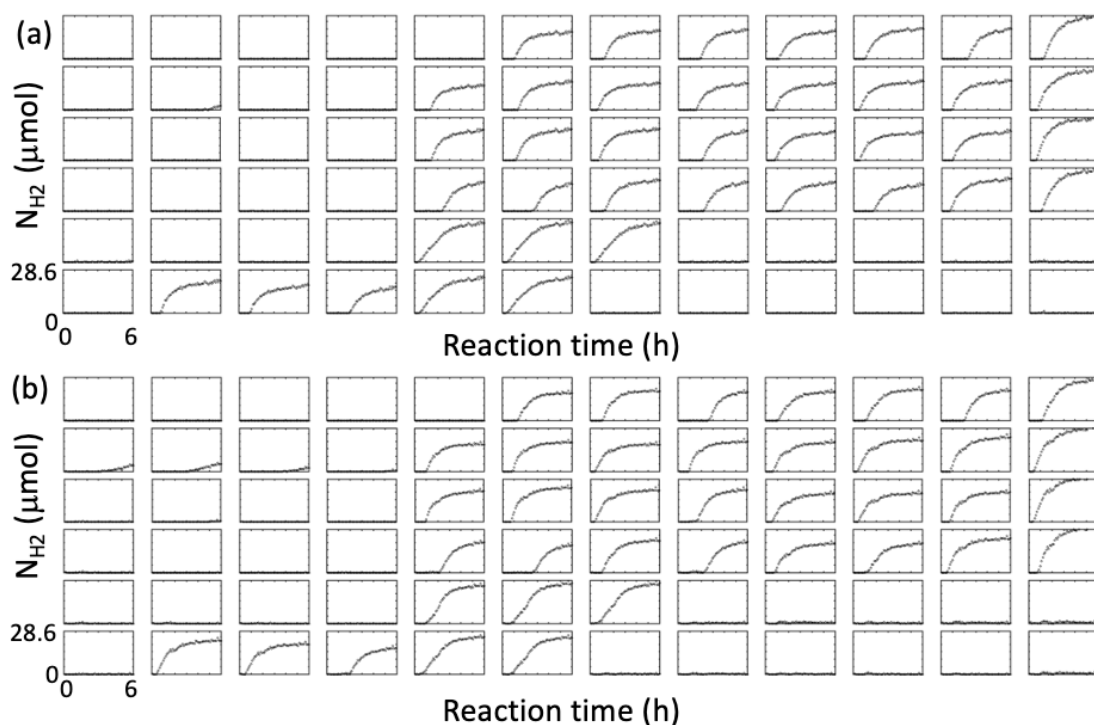


Figure S8. The amount of hydrogen in each vial of reactor Array 3. Each rectangle represents one of the vials in Fig. S6 and the contents are described in Table 2. Each graph has a domain of 0 to 6 h on the horizontal axis and 0 to 28.6 μmol hydrogen on the vertical axis. (a) First 6 h reaction. (b) Second 6 h reaction.

	SS-S010	SS-S110	SS-S210	SS-S310	SS-S010T	SS-S110T	SS-S210T	SS-S310T	S010T	S110T	S210T	S310T
pH = 2						2136	2441	2450	2048	2205	2354	2914
pH = 6	344				2193	2862	2956	2847	2649	3381	2962	3944
pH = 9					2729	4024	3462	2724	2408	3039	2731	4335
pH = 12					2184	1991	2485	2306	2111	2016	3796	4879
shell					2132	2132	2033					
faceted	3343	3086	1679		2192	1862						

Figure S9. Mass specific rates of hydrogen production from Array 3 for the second run. Cells with no numbers did not produce hydrogen above the detectible limit. In other cells, the number is $\mu\text{mol}/(\text{g}\cdot\text{h})$. As a guide to the eye, each cell is colored from white to red such that the minimum value is white and the maximum value is the darked red. Based on the five identical samples (platinized P25 TiO_2), the average \pm standard deviation is $2079 \pm 130 \mu\text{mol}/(\text{g}\cdot\text{h})$.

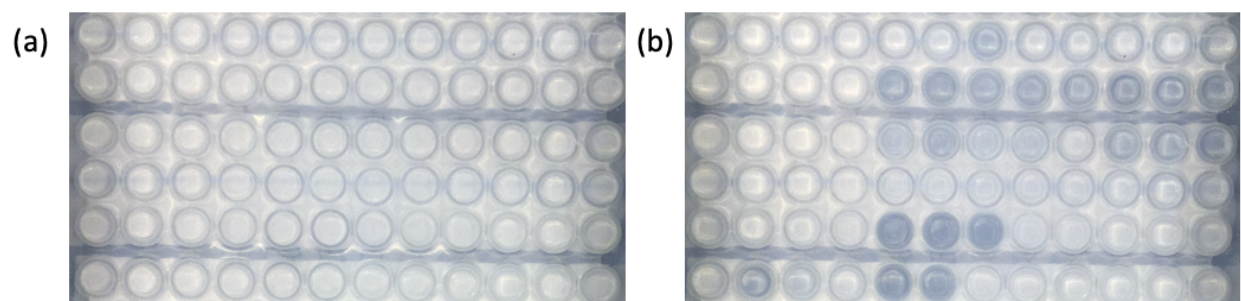


Figure S10. The pictures of reactor Array 4 (a) before and (b) after a 16.5 h run while illuminated by 400 nm light. The image looks down on the hydrogen sensitive tape. The intensity of the color change is related to the hydrogen concentration. (c) before and (d) after the second 16.5 h run.

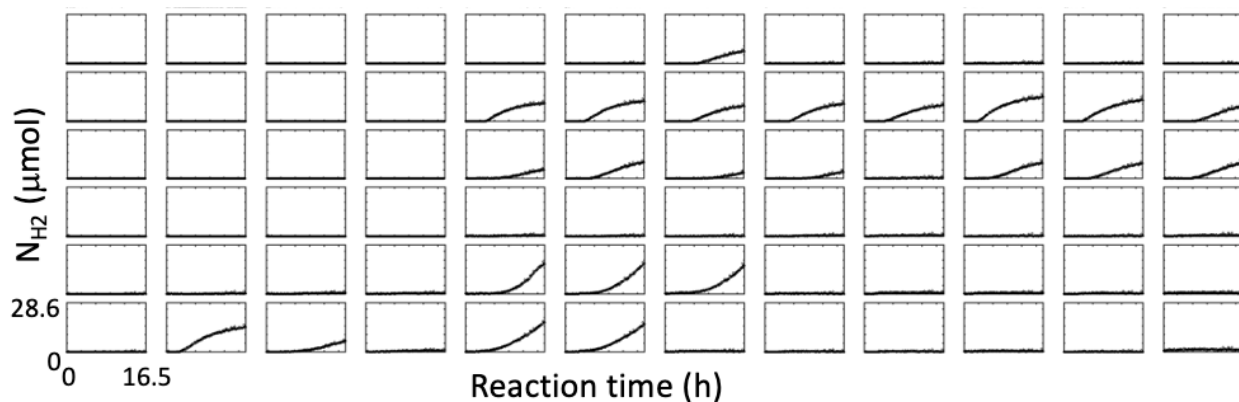


Figure S11. The amount of hydrogen in each vial of reactor Array 4 while illuminated by 400 nm light. Each rectangle represents one of the vials in Fig. S10 and the contents are described in Table 2. Each graph has a domain of 0 to 16.6 h on the horizontal axis and 0 to 28.6 μmol hydrogen on the vertical axis.